Earth and Planetary Science Letters 446 (2016) 56–67

Contents lists available at ScienceDirect

Earth and Planetary Science Letters

www.elsevier.com/locate/epsl

Argon, oxygen, and boron isotopic evidence documenting $^{40}Ar_E$ accumulation in phengite during water-rich high-pressure subduction metasomatism of continental crust

Carrie A. Menold [a,c,*], Marty Grove [b], Natalie E. Sievers [b], Craig E. Manning [c], An Yin [c], Edward D. Young [c], Karen Ziegler [c,d]

[a] Department of Geology, Albion College, 611 E. Porter St., Albion, MI, 49224, USA
[b] Department of Geological & Environmental Sciences, Stanford University, Palo Alto, CA, 94305, USA
[c] Department of Earth & Space Science, University of California, Los Angeles, CA, 90095, USA
[d] Department of Earth & Planetary Sciences, University of New Mexico, Albuquerque, NM, 87131, USA

ARTICLE INFO

Article history:
Received 20 November 2015
Received in revised form 5 April 2016
Accepted 9 April 2016
Available online xxxx
Editor: B. Marty

Keywords:
$^{40}Ar/^{39}Ar$
$\delta^{18}O$
$\delta^{11}B$
high-pressure
excess ^{40}Ar
phengite/fluid partition coefficient for Ar

ABSTRACT

The Luliang Shan area of the North Qaidam high pressure (HP) to ultrahigh pressure (UHP) metamorphic terrane in northwestern China features thick, garnet- and phengite-rich metasomatic selvages that formed around gneiss-hosted mafic eclogite blocks during HP conditions. Here we present new $^{40}Ar/^{39}Ar$, $\delta^{18}O$, and $\delta^{11}B$ results from a previously studied 30 m, 18 sample traverse that extends from the host gneiss into a representative eclogite block. Previous thermobarometry and new mica-quartz oxygen isotope thermometry from the traverse reveal that the phengite-rich selvage formed at temperatures similar to those recorded by the eclogites at peak pressure. Quartz and white mica $\delta^{18}O$ data from the selvage cannot be explained by simple mixing of gneiss and eclogite, and indicate a fluid/rock ratio >1 during regional-scale infiltration of high $\delta^{18}O$ (ca. 14‰) fluids. Heavy $\delta^{18}O$ overgrowths of metamorphic zircon over lighter $\delta^{18}O$ detrital grains indicate that the gneiss was similarly affected. Starkly contrasting boron content and $\delta^{11}B$ compositions for the host gneiss and the selvage also cannot be explained by local-scale devolatilization of the gneiss to form the selvage. Instead, the boron systematics are best attributed to two distinct phases of fluid infiltration: (1) low-boron selvage phengite with $\delta^{11}B$ from −10 to −30‰ grew under HP conditions; and (2) tourmaline and boron-rich muscovite with generally positive $\delta^{11}B$ crystallized in the host gneiss under subsequent lower pressure epidote–amphibolite facies conditions as the Luliang Shan gneiss terrane was exhumed past shallower portions of the subduction channel. Consistent with observations made worldwide, we were able to identify uptake of excess argon ($^{40}Ar_E$) in phengite as a high pressure phenomenon. Phengite $^{40}Ar/^{39}Ar$ ages from massive eclogite exceed the ca. 490 Ma zircon U–Pb age of eclogite metamorphism by a factor of 1.5. However, phengite ages from the more permeable schistose selvage were even older, exceeding the time of eclogite formation by a factor of 1.7. In contrast, lower pressure retrograde muscovite present within the host gneiss and in discrete shear zones cutting the selvage yield $^{40}Ar/^{39}Ar$ ages that were younger than the time of HP metamorphism and consistent with regional cooling age patterns. Our observation of high $^{40}Ar_E$ concentrations in phengite from schistose rocks infiltrated by regionally extensive fluids at HP conditions runs contrary to widely held expectations. Conventional wisdom dictates that low phengite/fluid partition coefficients for argon ($D^{Ar}_{phg/fluid} = 10^{-3}$ to 10^{-5}) coupled with the dry, closed systems conditions that are widely reported to characterize HP metamorphism of continental crust explains why high concentrations of $^{40}Ar_E$ partitions are able to accumulate within phengite. We alternatively propose that phengite/fluid partition coefficients for argon increase linearly with pressure to values as high as 10^{-2} to allow phengites to accumulate large amounts of $^{40}Ar_E$ from aqueous fluids under HP to UHP conditions.

1. Introduction

Two dramatically different conceptualizations exist for the scale of fluid flow during subduction-related high pressure (HP) meta-

* Corresponding author at: Department of Geology, Albion College, 611 E. Porter St., Albion, MI, 49224, USA. Tel.: +1 517 629 0312.
E-mail address: cmenold@albion.edu (C.A. Menold).

http://dx.doi.org/10.1016/j.epsl.2016.04.010
0012-821X/

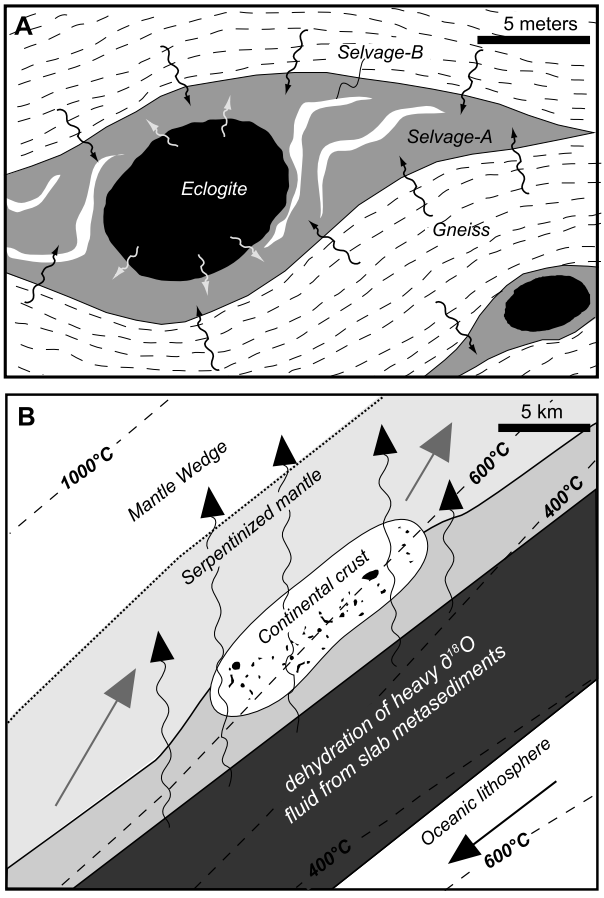

Fig. 1. Schematic illustrations of the scale of fluid flow during high pressure (HP) to ultra-high pressure (UHP) metamorphism of continental crust. A. Local (meter-scale) derivation of fluid from adjacent lithologies. B. Regional fluid flow transferring fluids from the subduction zone upwards towards the mantle hangingwall.

morphism. In the case of subducted continental crust, a wide range of petrographic, fluid-inclusion, Nd–Sr and C–O–H stable isotope data have indicated that the length scale of fluid transport during HP metamorphism is typically limited (0.001 to 1 m) even for deformed rocks (e.g., Rumble and Yui, 1998; Cosca et al., 2005; Warren et al., 2012; Smye et al., 2013) (see Fig. 1A). In contrast, there is no doubt that extensive migration of metasomatic fluids derived from devolatilization of subducted oceanic crust and overlying sediment occurs over 10s of kilometers under HP to UHP conditions to hydrate and flux arc magmatism within the overlying lithospheric mantle (e.g., Ishikawa and Nakamura, 1994; Iwamori, 1998; Schmidt and Poli, 1998; Manning, 2004; Bebout, 2007; Cagnioncle et al., 2007; Till et al., 2012) (see Fig. 1B). Even if both conceptualizations are fundamentally correct for continental vs. oceanic subduction respectively, there should be instances where small volumes of continental crust is subducted during the early stage of continental collision where the subducting plate is still fundamentally oceanic in character. In this instance, a small, subducted mass of continental crust might still experience regional fluid flow from the subducted oceanic slab (Fig. 1B).

Initial subduction of relatively small volumes of continental crust prior to final closure of an ocean basin has been reported for a number of large collisional orogens (e.g., Kylander-Clark et al., 2012). In this paper, we evaluate the scale of fluid mobility within a ca. 100 km^2 exposure of continental crust metamorphosed to near-UHP conditions. Available data indicate that the Luliang Shan massif shown in Fig. 2 represents the earliest subducted continental rocks of the North Qaidam ultrahigh-pressure (UHP) metamorphic terrane in northwestern China (Zhang et al., 2013). Garnet- and phengite-rich selvages mantling eclogite are a ubiquitous feature throughout the Luliang Shan study area and formed at near-peak pressure conditions (Menold et al., 2009). These selvages offer the opportunity to study the nature of fluid–rock interactions during the earliest stages of continental subduction.

Coupled argon, oxygen, and boron isotopic measurements provide a useful approach to assess fluid/rock interactions under HP conditions (e.g., Cosca et al., 2005; Smye et al., 2013; Halama et al., 2014). Because the concentration of oxygen is high in both rocks and fluids, the oxygen isotopic composition of minerals within the host gneiss, selvage, and eclogite can be used to help constrain the mass balance related to fluid-mediated metasomatism. Conversely, both boron and argon are strongly partitioned into the fluid phase. Boron concentrations and isotope ratios in phengite are sensitive to devolatilization history and fluid/rock interactions (Marschall et al., 2007) and phengite characteristically hosts most of the boron present in rocks (Bebout, 2007). Similarly, argon can also be used as a trace element to track fluid/rock interactions (Kelley, 2002) and phengite is the principal host of $^{40}Ar_E$ in HP rocks (Scaillet, 1998). Intergranular fluids have high argon solubilities and can, under appropriate conditions, serve either as a source or sink of ^{40}Ar to minerals (e.g., Baxter et al., 2002). In this study, the term excess ^{40}Ar ($^{40}Ar_E$) is used for all non-atmospheric ^{40}Ar that is incorporated into minerals by processes other than *in-situ* radioactive decay of ^{40}K. Based upon predicted low phengite/fluid partition coefficients for argon (e.g., 10^{-3} to 10^{-6}; Kelley, 2002), there is a well-established expectation that high concentrations of $^{40}Ar_E$ in phengite indicate stagnant, fluid-poor conditions (e.g., Cosca et al., 2005; Smye et al., 2013). By integrating argon, oxygen, and boron isotopic data from the hydrated eclogite selvages from the Luliang Shan terrane, we can evaluate the sources and scale of fluid flow during selvage formation.

2. Geologic background

Exposures of the early Paleozoic North Qaidam UHP metamorphic terrane are discontinuously exposed along the northern margin of Qaidam Basin in northern Tibet (Fig. 2, inset). The exposure pattern of the North Qaidam UHP terrane is controlled by Cenozoic faults that thrust HP to UHP rocks over Tertiary and even Quaternary sediments (Yin et al., 2008). Thermobarometric and mineral inclusion studies from throughout the North Qaidam report UHP conditions (see reviews by Mattinson et al., 2007; Zhang et al., 2013). However, estimates of temperature at peak pressure vary considerably for different exposures throughout the North Qaidam terrane, ranging from 605 to 1000 °C. The timing of UHP (or near UHP) metamorphism for these individual exposures spans a similarly broad range from 488 to 420 Ma (see reviews by Mattinson et al., 2007; Zhang et al., 2013).

2.1. Luliang Shan (Yuka) area

This study was performed with rocks of the Luliang Shan (also called Yuka) locality (Figs. 2, 3). The Luliang Shan records the earliest and coolest conditions of HP metamorphism of all of the exposures found throughout the North Qaidam terrane (Menold et al., 2009; Zhang et al., 2013). The HP rocks of the Luliang Shan are situated beneath a regionally extensive mylonitic shear zone (Fig. 2). Rocks beneath the shear zone are foliated but not sheared. Four stages of deformation can be recognized (Yin et al., 2007): (1) penetrative deformation which occurred prior to and during HP metamorphism; (2) partial exhumation of the Luliang Shan as a coherent block beneath the shear zone that structurally overlies the terrane; (3) a regionally extensive epidote–amphibolite facies foliation overprinting all pre-Devonian units; and (4) a more recent Cenozoic deformation ultimately exhuming the Luliang Shan

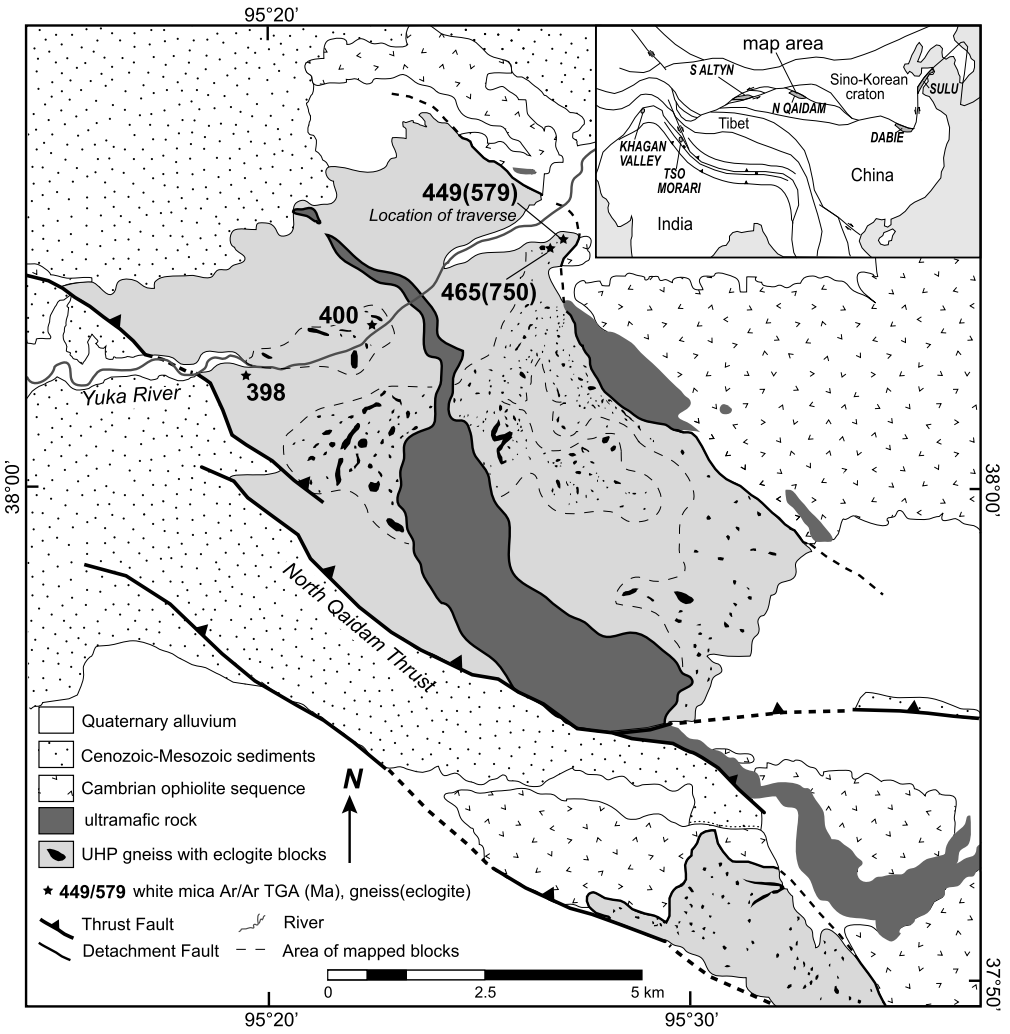

Fig. 2. A geologic map of the Luliang Shan locality based on mapping by C.A. Menold with assistance from M. McRivette, A. Robinson, A. Yin and X.H. Chen in 2000, 2002 and 2004 (modified from Menold et al., 2009). $^{40}Ar/^{39}Ar$ ages are from white mica obtained from gneiss. The dashed line encloses an area where the approximate size and shape very large eclogite blocks were each mapped. Inset shows the location of the field area relative to other UHP terranes in Asia.

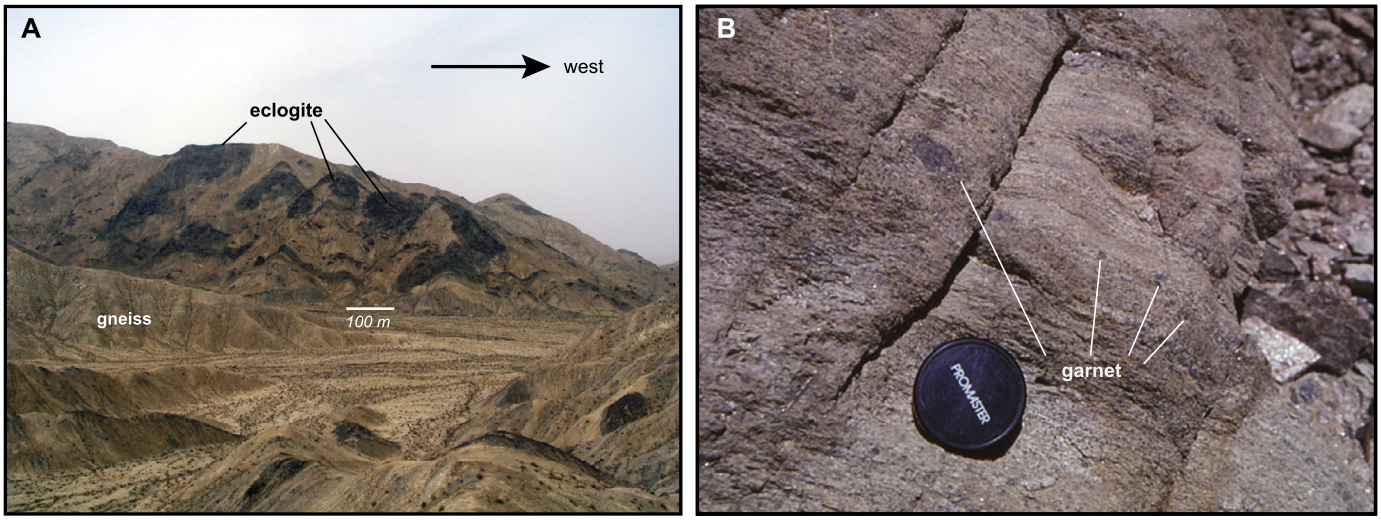

Fig. 3. Field photos of the Luliang Shan region. A. View of eclogite-bearing gneiss showing the typical distribution of eclogite blocks in the host gneiss. Modified from Menold et al. (2009). B. Close up of a garnet-mica rich selvage (CM 7/17/02-5).

to the surface. Removal of the effects of Cenozoic deformation would restore the regional foliation within the Luliang Shan to a sub-horizontal orientation (Yin et al., 2007).

Fig. 4 shows the locations of 18 samples previously described by Menold et al. (2009) along a 30 m traverse across the contact between an eclogite block and surrounding host gneiss. The rocks

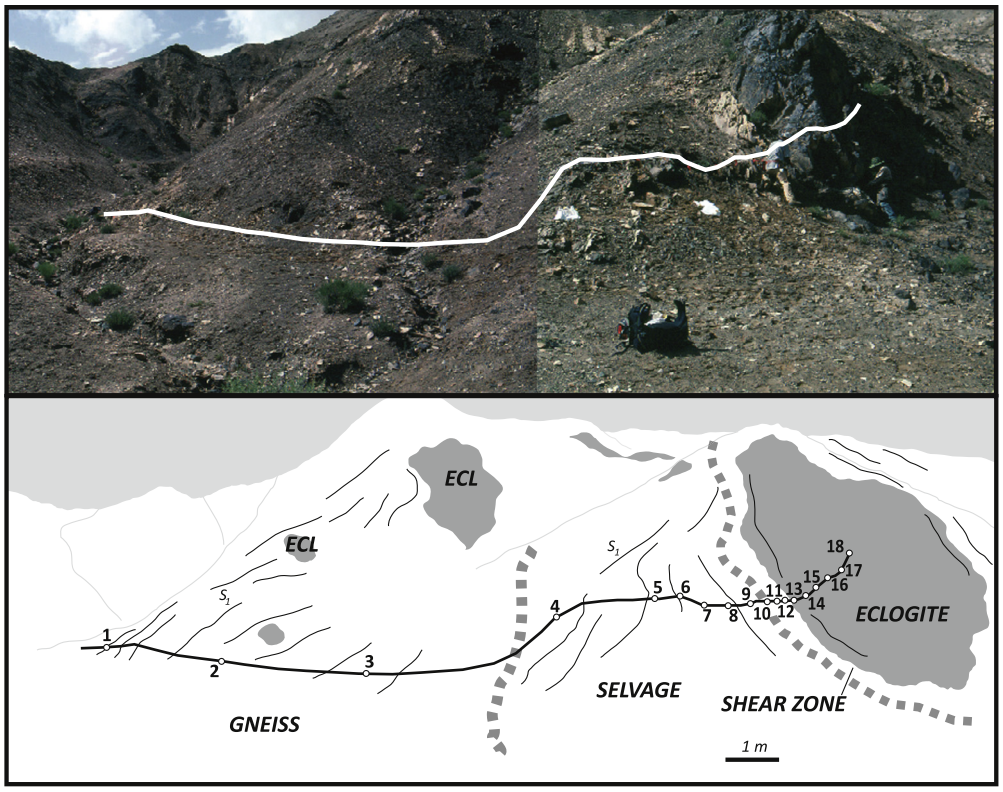

Fig. 4. Photo and cartoon rendering of the sample traverse with numbered sample locations. Samples were collected along the line. Approximate boundaries between lithologic and structural zones shown with dashed lines.

were most densely sampled within three meters of the contact. The traverse can be divided into four zones: (1) coarse-grained host gneiss (samples CM 7/17/02-1 to -3); (2) the schistose garnet-muscovite selvage (CM 7/17/02-4 to -10); (3) a narrow shear band of fine-grained biotite-muscovite schist in the selvage rocks at the eclogite contact (CM 7/17/02-11 to -12); and (4) mafic eclogite (CM 7/17/02-13 to -18). Below we provide additional background information about each of these lithologies.

2.1.1. Gneiss

Quartz-rich gneiss is very well exposed throughout the Luliang Shan (Figs. 3, 4). The gneiss protolith remains uncertain and could be of igneous, sedimentary, or mixed origin (Gehrels et al., 2003; Zhang et al., 2013). Compositionally, samples of the gneiss from the traverse plot in the granite/arkose field in an AKF projection (Fig. 5A). Zircon U–Pb ages measured from the host gneiss are >928 Ma (Gehrels et al., 2003). The gneiss lacks obvious evidence of HP metamorphism and may not have recrystallized at high pressure (e.g., Proyer, 2003; Massonne, 2009). Significant recrystallization did occur, however, during the development of the regionally extensive epidote amphibolite fabric that is primarily expressed by muscovite (Fig. 3). Muscovite $^{40}Ar/^{39}Ar$ cooling ages indicate exhumation of the host gneiss to shallow crustal levels occurred by 470–450 Ma (see cooling age trend in Fig. 2; Zhang et al., 2005). By 445 Ma, regionally extensive granitoids had intruded all of the pre-Devonian units (Gehrels et al., 2003).

2.1.2. Eclogite

The gneiss hosts numerous masses of mafic eclogite (Figs. 2, 3A). Small eclogite blocks (1 to 10 m in maximum dimension) are ovoid. Larger eclogites occur as lensoidal masses that are 10 to 100s of meters in length and locally isoclinally folded (e.g., Mattinson et al., 2007; Yin et al., 2007; Menold et al., 2009; Zhang et al., 2013). Field relations indicate that the eclogite boudins originated as basalts dikes that intruded the gneiss. Whole rock analyses of the eclogite collected along the traverse plot in the basalt field in an AKF projection (Fig. 5A; Table DR1, 2). Zircon U–Pb geochronologic studies indicate that eclogite facies metamorphism in the Luliang Shan occurred at ca. 480–490 Ma (Yang et al., 2002; Zhang et al., 2005, 2009). Estimates of peak pressure for the Luliang Shan eclogite are 2.5 GPa at 590 °C, followed by heating of ca. 50 °C during early decompression (Menold et al., 2009; Zhang et al., 2009). These thermobarometric results suggest peak conditions were just below the coesite stability field. While coesite has been observed in other exposures throughout the North Qaidam UHP terrane, no coesite has been observed in the locality we have studied in the Luliang Shan. The eclogite is medium- to coarse-grained and generally preserves an eclogite facies assemblage (garnet + omphacite + rutile + quartz ± phengite ± zoisite) in the block interiors. Coarse phengite from the interior of the block has 3.35–3.50 Si per formulat unit (p.f.u.), while phengite from the margin is less celadonitic (~3.25 Si p.f.u.) (Table DR3). While most sampled portions of the eclogites are nearly anhydrous, hydration of the eclogite block margins produced H_2O contents up to 6.5 wt% (Menold et al., 2009).

2.1.3. Selvage

Distinctive schistose garnet + mica-rich selvages up to 10 m thick surround most eclogite blocks throughout the Luliang Shan (Figs. 1A, 4B). As indicated in Fig. 5A, the Luliang Shan selvage samples fall into two compositional groups. “Selvage-A” samples are enriched in garnet and phengite and plot between the compositions of the eclogite and the host gneiss. Modes of garnet and white mica in the selvage-A samples are a factor of five higher than the background abundance of these phases in the gneiss (Menold et al., 2009). Alternatively, “selvage-B” samples compositionally resemble the host gneiss (Fig. 5A). Other phases present include quartz + plagioclase + ilmenite ± epidote ±

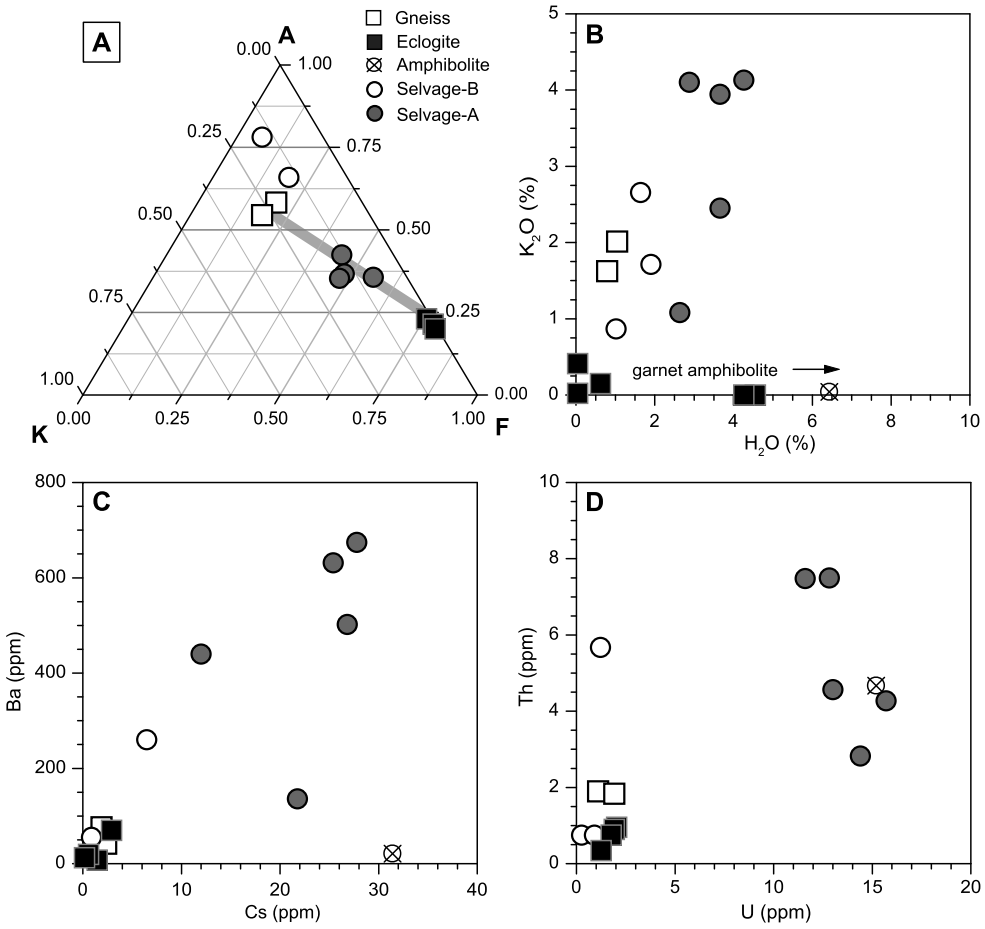

Fig. 5. Geochemistry of traverse samples. A. AKF projection of whole rock analyses. Note two types of selvage samples. Garnet and phengite-rich selvage analyses (selvage-A) fall along a mixing line between the compositions of host gneiss and eclogite. Quartzofeldspathic samples (selvage-B) plot with host gneiss. B. Whole rock H_2O (inferred from loss on ignition data) vs. K_2O. All selvage samples are enriched in these components relative to the host gneiss and eclogite. C. Whole rock Cs vs. Ba. Selvage samples tend to have far higher concentrations than either the host gneiss or eclogite. D. Whole rock U vs. Th. Selvage samples tend to have far higher concentrations than either the host gneiss or eclogite. See Table DR2 for complete table of whole-rock compositions.

apatite ± kyanite ± allanite ± titanite. Previous petrologic and thermobarometric studies in the Luliang Shan indicate that the mineral assemblages in both the selvage and the mafic eclogite are isofacial and formed during prograde to near-peak pressure metamorphism (Mattinson et al., 2007; Menold et al., 2009; Zhang et al., 2013). Petrologic analysis and calculation of pseudosections indicate that the selvage formed at 26 kbar and 605 °C (Menold et al., 2009). A range of textural occurrences of white mica occurs within the selvage (Menold et al., 2009); including phengite with up to 3.4 Si p.f.u. included in garnet. Most selvage phengites have 3.20–3.30 Si p.f.u., are not strongly zoned, and occur as large (~1 mm), variably oriented grains in the schistose matrix. In some cases, finer-grained muscovite (3.05–3.13 Si p.f.u.) associated with chlorite and biotite locally replace garnet and the coarse phengite. The most muscovite-rich micas (<3.10 Si p.f.u.) occur along with paragonite in a shear zone formed within the selvage near the eclogite contact.

3. Methods

3.1. Argon isotope methods

Seventeen ca. 5 mg samples of white mica were hand-selected from purified concentrates obtained using standard shape, density, and magnetic separation techniques for $^{40}Ar/^{39}Ar$ measurements at UCLA. Point counting revealed that the proportions of phengite, paragonite, and muscovite components vary in the traverse samples (Menold et al., 2009). Muscovite prevails within the gneiss and within the shear zone while phengite predominates within the selvage and the eclogite. One sample (CM7/17/02-14) from the eclogite lacked sufficient mica for analysis. Micas were hand-selected, packed in Cu foil, and co-irradiated with Fish Canyon sanidine flux monitors (28.04 ± 0.08 Ma; Jourdan and Renne, 2007) in the L67 position of the University of Michigan's Ford reactor for 45 h. Samples were incrementally outgassed in a double vacuum resistance furnace and fully-automated, all-metal extraction line (Lovera et al., 1997). Measurements were performed with a VG 1200S mass spectrometer using an electron multiplier in analogue mode (argon sensitivity of 1.2×10^{-16} mol/mV). Corrections for mass discrimination were based upon measurement of purified atmospheric argon which yielded $^{40}Ar/^{36}Ar$ values of 293.5 ± 0.5. Representative total mass spectrometer and static extraction line blanks were 3×10^{-16} mol, 4×10^{-17} mol, 2×10^{-17} mol, 4×10^{-17} mol, and 2×10^{-17} mol for m/e 40, 39, 38, 37, and 36 amu respectively. Measured argon isotopic ratios were corrected for backgrounds, abundance sensitivity, mass discrimination, radioactive decay, and nucleogenic interferences. Age uncertainties are reported at the 1σ level, and do not include uncertainties in J-factor, irradiation correction factors, or decay constants. A summary of the $^{40}Ar/^{39}Ar$ results including sample plots and data tables appears in the data repository (Table DR4).

Table 1
Isotopic data from traverse samples.

Sample	m	Mineral	Total gas age		White mica $d^{18}O'$	Quartz $d^{18}O'$	$\Delta^{18}O_{qtz\text{-}ms}$	T (°C)
			Ma	St. dev.				
CM7/17/02-1[a]	23	White mica	475.5	6.9	10.91	14.28	3.4	545
CM7/17/02-2	17	White mica	437.1	6.5	11.25	14.63	3.4	544
CM7/17/02-3	12	White mica	466.7	7.2	12.17	15.17	3.0	587
CM7/17/02-4	5	White mica	823.9	11.9	11.40	13.33	1.9	758
CM7/17/02-5	3	White mica	503.2	8.6	12.88	15.45	2.6	646
CM7/17/02-6	2.5	White mica	770.8	10.6	11.60	14.35	2.8	620
CM7/17/02-7	2	White mica	699.6	15.6	12.17	15.13	3.0	592
CM7/17/02-8	1.5	White mica	739.4	11.4	11.36	13.90	2.5	651
CM7/17/02-9	1	White mica	609.9	9.3	11.98	15.51	3.5	531
CM7/17/02-10	0.5	White mica	480.4	7.8	11.38	14.49	3.1	575
CM7/17/02-11	0.25	White mica	463.9	7.2	10.38	13.06	2.7	630
CM7/17/02-12	0.05	White mica	418.5	12.8	9.92			
CM7/17/02-13	−0.1	White mica	631.5	9.0	9.91			
CM7/17/02-15	−0.5	White mica	729.3	11.9		11.93		
CM7/17/02-16	−1	White mica	750.1	10.9	8.62			
CM7/17/02-17	−1.5	White mica	658.5	11.4	7.81	10.57	2.8	618
CM7/17/02-18	−3	White mica	611.5	10.2				

[a] Complete data table for argon and oxygen isotope analyses in the data repository (Tables DR4, DR5).

3.2. Oxygen isotope methods by laser fluorination

White mica and quartz were hand-selected from purified concentrates to produce ca. 2 mg bulk aliquots for oxygen isotopic measurements at UCLA. High-precision oxygen-isotope analyses were made using a 25 W CO_2 laser attached to a laser-fluorination (F_2-gas) vacuum extraction line. Molecular oxygen was released from the samples by the laser-assisted fluorination, producing molecular O_2 and solid fluorides. Excess F_2 was removed from the produced O_2 by reaction with hot KBr. The oxygen was purified by freezing to a 13X molecular sieve at −196 °C followed by elution of the O_2 from the first sieve at −131 °C to a second 5 Å molecular sieve at −196 °C (Young et al., 1998). Measurements of the isotope ratios were made on a Finnigan Delta-Plus™ dual inlet isotope ratio mass spectrometer, and the oxygen isotope ratios are calibrated against the isotopic composition of air O_2 and San Carlos (SC) olivine. Each sample gas was analyzed multiple times, each analysis consisting of 20 cycles of sample-standard comparison. Calculated $\delta^{18}O$ values refer to the per-mil deviation in a sample ($^{18}O/^{16}O$) from SMOW, expressed as $\delta^{18}O = [(^{18}O/^{16}O)_{sample}/(^{18}O/^{16}O)_{SMOW} - 1] * 10^3$. The delta-values were converted to linearized values by calculating: $\delta^{18}O' = \ln[(\delta^{18}O + 10^3)/10^3] * 10^3$ in order to create straight-lined mass-fractionation curves. SC olivine standards (1–2 mg) were analyzed daily. The average values of 28 olivine grains analyzed during the same time period as the samples are $\delta^{18}O' = 5.25‰$ (0.034 s.e.).

3.3. Oxygen isotope methods by ion microprobe

Zircons from the gneiss (CM7/17/02-1, CM7/17/02-3) were hand selected, mounted, sectioned, and polished in epoxy. Selected grains were then analyzed for high spatial resolution $\delta^{18}O$ zircon determination using the UCLA CAMECA ims 1270 high-resolution ion microprobe in Faraday multicollection mode following the methods of Trail et al. (2007). In all analyses a liquid nitrogen cold finger was used to remove trace condensable gases from the sample chamber. A ∼5 nA Cs+ beam was focused to a ca. 20 μm spot and 10 keV secondary ions were admitted to the mass spectrometer after passing through a 30 eV energy slit. Zircons were presputtered for 1 min, and the total integration time per analysis was 5 min. Instrumental mass fractionation was determined from repeated analysis of AS-3 zircon standard ($\delta^{18}O = 5.43‰$). The external uncertainty from repeated analysis of AS-3 during the analytical session is 0.28‰ (1 s.d.).

3.4. Boron isotope methods

Boron concentration data and $^{11}B/^{10}B$ ratios were measured by ion microprobe methods using the Stanford-USGS SHRIMP-RG instrument. A near Kohler, 3 nA primary O^{2-} beam used for analysis produced a ca. 20–25 μm diameter × 2 μm deep sputter pit in the 24 min required for an analysis. Helmholtz coil settings were optimized to offset stray magnetic fields in the source to ensure proper secondary alignment of the ^{10}B and ^{11}B ion beams. High resolution mass scans indicated no measurable overlapping mass interferences. Measurements were performed with 6000 mass resolution at 10% peak height. Thirty cycles of measurements were acquired from the NIST SRM-611 standard using counting times of 20 and 10 s for ^{10}B and ^{11}B. For the unknown, counting times were reduced to 15 and 8 s due to higher boron intensities. All measurements were acquired in monocollection mode using an ion counting discrete dynode detector with a dead time of 25 ns. The mean of all $^{11}B/^{10}B$ measurements from the standards ($n = 52$) averaged 3.876 ± 0.005 1 s.d. (1.2‰). We normalized the $^{11}B/^{10}B$ ratio measured for unknowns with the accepted value of 4.04152 for NIST SRM-611 (Brand et al., 2014).

4. Results

4.1. Argon isotope results

Total gas $^{40}Ar/^{39}Ar$ ages are summarized in Table 1 and plotted in Fig. 6A. Complete data tables, age spectra, and inverse isochron plots are provided in the data repository (Figs. DR1, 2; Table DR4). The character of the age spectra determined for mica samples along the traverse varies considerably. Muscovite from the gneiss (samples CM7/1/702-1 to -3) yield smoothly varying release spectra (data repository for release spectra for each sample) and total gas (i.e., K–Ar) ages (TGA) ranging from 437 to 475 Ma (Fig. 6A). These ages are consistent with regional trends in $^{40}Ar/^{39}Ar$ muscovite total gas ages determined for the gneiss throughout the Yuka region (see representative total gas ages in Fig. 1). In contrast, mixtures of phengite with subordinate retrograde muscovite from the schistose selvage (CM7/17/02-4 to -9) yield erratic release spectra and 610–824 Ma total gas ages that exceed the 480–490 Ma time of eclogite facies crystallization by 100s of m.y. (Fig. 6A; Zhang et al., 2005). Some of the scatter may be due to differences in grain size and argon retention properties of high-pressure phengite and retrograde muscovite present within the white mica concentrates. The youngest of these samples

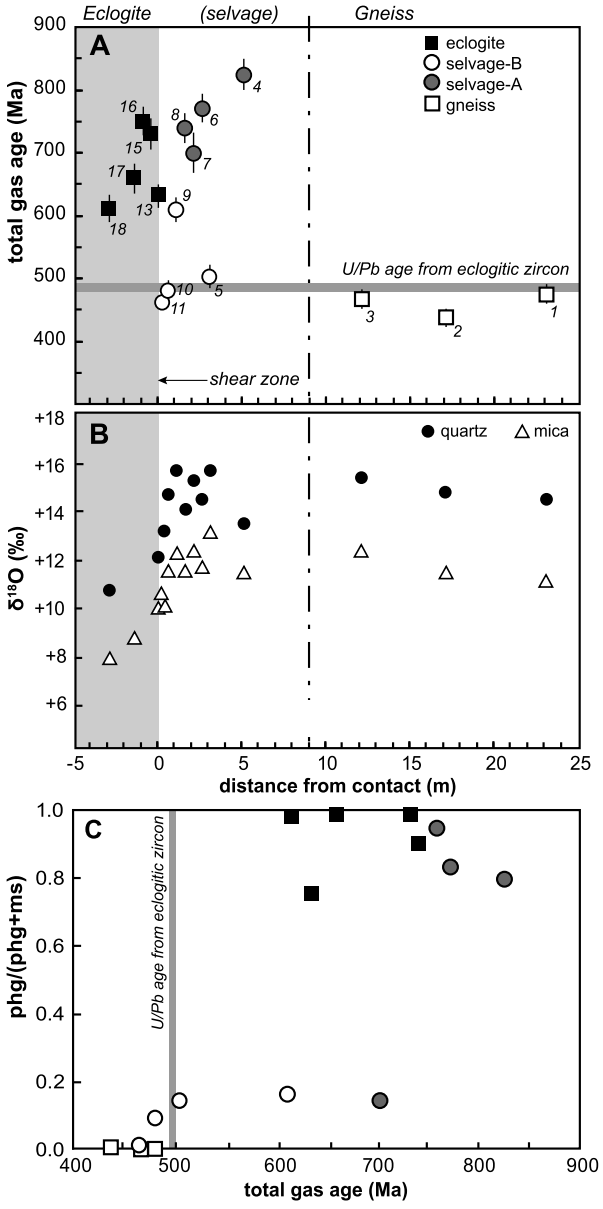

Fig. 6. Argon and oxygen isotopic data from the traverse. A. Total gas $^{40}Ar/^{39}Ar$ age vs. distance from the eclogite–gneiss contact. Sample numbers and age of eclogite facies metamorphism included for reference (Zhang et al., 2005, 2013). Phengite ages for the selvage samples and eclogite greatly exceed the U–Pb zircon age for eclogite metamorphism while muscovite ages from the host gneiss and shear zone overprinting the selvage are younger than the timing of eclogite metamorphism. B. Oxygen isotope data from quartz and white mica concentrates versus distance along the traverse. The selvage samples yield the highest $\delta^{18}O$ values. C. Proportion of phengite as calculated by point counting vs. total gas age. Point counting data for the traverse taken from Menold et al. (2009).

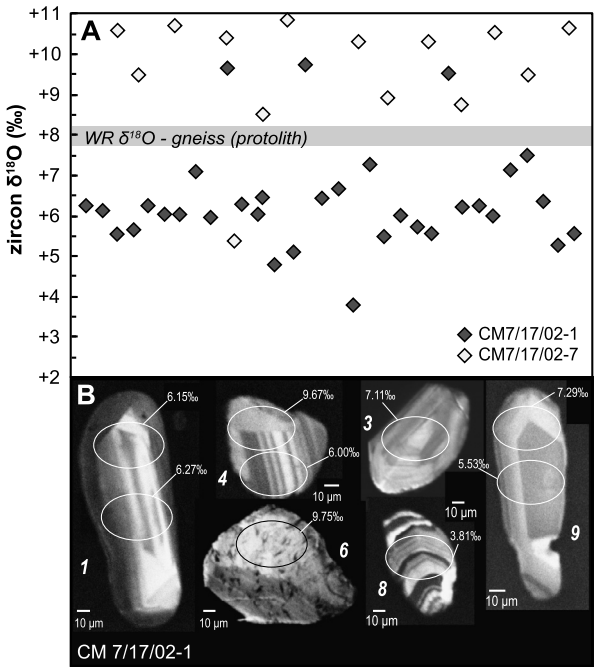

Fig. 7. A. Ion microprobe oxygen isotopic data from the host gneiss. Results from CM 7/17/02-1. Most zircon exhibits growth zoning with metamorphic rims locally present (see inset). The average $\delta^{18}O$ of 28 zircon interiors was 5.8 ± 1.0‰. Three rims overgrowths averaged 9.7 ± 0.2%. Results from host gneiss sample CM 7/17/02-7. Nearly all zircon present is metamorphic in origin. Seventeen analyses yielded a $\delta^{18}O$ value of 9.0‰. Since zircon yields $\delta^{18}O$ values that are ca. 3‰ lighter than quartz (Trail et al., 2007), the metamorphic zircon rim values are consistent with a quartz $\delta^{18}O = 12$ to 13‰ for the two samples. B. Cathodoluminescence images of zircon grains from CM7/17/02-1 with oxygen data.

(CM7/17/02-5) is strongly sheared. The mylonitic, muscovite-rich samples within the shear zone along the contact with the eclogite block (CM7/17/02-10 to -12) exhibit smoothly varying age spectra and total gas $^{40}Ar/^{39}Ar$ ages of 454 ± 5 Ma that, within error, overlap muscovite ages determined for the gneiss (Fig. 6A). Finally, phengite-dominated samples from within the eclogite yield erratic age spectra and anomalously old total gas $^{40}Ar/^{39}Ar$ ages in excess of 600 Ma (Fig. 6A; Fig. DR1).

4.2. Oxygen isotope results

Quartz and muscovite oxygen isotope results are tabulated in the data repository (Table DR5), while a summary of the data appears in Table 1. As shown in Fig. 6B and Table 1, $\delta^{18}O$ values measured from muscovite-rich white mica concentrates from the gneiss increase from 10.9‰ to 12.2‰ toward the selvage; coexisting quartz increases from 14.3‰ to 15.2‰ over the same distance. White mica concentrates within the selvage vary from 11.4‰ to 12.9‰, while coexisting quartz vary from 13.3‰ to 15.5‰ (Fig. 6B). Near the sheared contact with the eclogite, $\delta^{18}O$ values decrease to between 9.9 and 10.4‰ for white mica concentrates and to between 11.9‰ and 13.1‰ for quartz. The lowest $\delta^{18}O$ quartz value (10.6‰) measured was within the eclogite block (Fig. 5B). Phengite within the eclogite yield 7.8‰ to 8.6‰ values. Overall, $\delta^{18}O$ values are ca. 2.5‰ lighter in the eclogite for both minerals relative to the gneiss.

Temperatures for quartz–white mica pairs were calculated using the fractionation data of Richter and Hoernes (1988) (Table 1). As previously mentioned, a variety of white mica compositions are present within the traverse samples. Oxygen isotope fractionation factors presented by Zheng (1993) indicate that muscovite, phengite, and paragonite all behave similarly. For simplicity, we have used muscovite–quartz fractionation data for all samples. Three quartz–muscovite pairs from the gneiss have $\Delta^{18}O_{qtz\text{-}ms}$ values of 3.0 to 3.4 producing model temperatures of 547–575 °C. Temperatures calculated for the less deformed selvage samples scatter significantly (550–765 °C). Samples from the contact shear zone have $\Delta^{18}O_{qtz\text{-}ms}$ values of 2.5 to 3.1 (550–630 °C).

Fig. 7A shows ion microprobe oxygen isotopes results from zircons from the gneiss and selvage (CM 7/17/02-1, CM 7/17/02-7). Tabulated results are presented in Table DR6 of the data repository. Zircon from the gneiss (CM7/17/02-1) exhibits subhedral overgrowths and internal zoning in cathodoluminescence (CL) images (Fig. 7B); anhedral grains that exhibits diffuse patchy CL zoning are also present (Fig. 7B). Analyses from the zoned population yields $\delta^{18}O$ values ($+5.8 \pm 1.0$‰) that are nearly 10‰ lower than quartz

(+14.3‰) from the same sample (Fig. 7A, 6B). Three analyses form the patchy, anhedral grains yields much higher $\delta^{18}O$ values of ca. 9.5‰ (Fig. 7A). Zircons from the selvage (CM7/17/02-7) are all anhedral and analyses from this population yield $\delta^{18}O$ values of 10.0 ± 0.8‰ (Fig. 7).

4.3. Boron isotope results

We acquired a total of 47 boron isotope measurements from samples CM 7/17/02-1 (host gneiss), CM 7/17/02-4 (retrograded selvage), CM 7/17/02-7 pristine selvage, and CM 7/17/02-11 (shear zone near eclogite contact). Tabulated results are presented in Table DR7 of the data repository. We acquired 20 measurements from muscovites in the host gneiss sample. Boron-contents and $\delta^{11}B$ values ranged from 3300 to 5500 ppm and from −2.4 to +8.4‰ respectively (Fig. 8). Eleven measurements were acquired from sample CM 7/17/02-4: eight analyses from phengite yielded boron-contents and $\delta^{11}B$ values ranged from 160 to 250 ppm and from −15.0 to −8.8‰ respectively and three retrograde muscovites yielded boron-contents and $\delta^{11}B$ values ranging from 70 ppm to 140 pm and from −26.4 to −15.0‰ (Fig. 8). Eight analyses from the more pristine selvage sample CM 7/17/02-7 yielded boron-contents and $\delta^{11}B$ values ranging from 50 to 230 ppm and from −28.7 to −6.5‰. Finally, seven analyses were obtained from shear zone muscovites in CM 7/17/02-11. Boron-contents and $\delta^{11}B$ values for these ranged from 500 to 2100 ppm and from −19.2 to −2.9‰; an additional measurement from paragonite in this sample fell within this range (Fig. 8).

5. Discussion

5.1. Evaluation of the extent of fluid flow during selvage formation

Considerable consensus has emerged in recent years that support very limited fluid flow and availability during the HP to UHP metamorphism of continental crust (e.g., Philippot, 1993; Rumble and Yui, 1998; Baxter et al., 2002; Cosca et al., 2005; Warren et al., 2012; Smye et al., 2013). Fig. 1A illustrates this end member model's view for the scale of fluid flow during selvage formation. As indicated, the fluid required to form the selvage at the gneiss/eclogite contact is considered to have originated locally from the host gneiss and/or possibly a hydrated basaltic protolith for the eclogite. Alternatively, the likelihood that the Luliang Shan gneiss terrane was subducted during the earliest stages of continental collision (e.g., Zhang et al., 2013) motivates a much different conceptual view for selvage formation. As shown in Fig. 2B, the selvage may have formed in response to regional infiltration of fluids that are well-known to flux arc magmatism in the overlying lithospheric mantle in non-collisional subduction zone settings (e.g., Ishikawa and Nakamura, 1994; Schmidt and Poli, 1998; Manning, 2004; Bebout, 2007; Till et al., 2012).

Selvage formation around mafic eclogite within the Luliang Shan took place either at, or shortly after attainment of peak pressure conditions. Menold et al. (2009) demonstrated that fluid-mediated metasomatism produced the selvages around mafic eclogite bodies at near peak pressure conditions. Menold et al.'s analysis indicated that mineral assemblages in both the eclogite and selvage experienced peak-pressure recrystallization at 25 ± 2 kbar and 590 ± 25 °C followed by decompression to peak temperature conditions at 18 kbar and 650 ± 25 °C. Stable isotope thermometry results from muscovite and phengite from the selvage reported in this study (607 ± 65 °C, Table 1) agree well with these temperatures during this initial phase of decompression.

The whole-rock chemistry of the selvage rocks strongly supports a significant role for fluid-mediated metasomatism during selvage formation (Fig. 5). As expected, components such as K_2O and water are highly enriched within the selvage relative to the gneiss or the eclogite (Fig. 5B). Similarly, the concentrations of fluid mobile trace elements such as cesium and barium (Fig. 5C) or uranium and thorium (Fig. 5D) are also much higher than can be explained by binary mixing of gneiss and eclogite (see Table DR1 in the data repository for complete whole rock compositions). Independent measurements of Li, Be, B, Rb, Sr, Cs, and Ba from the white micas present within the selvage and adjacent rocks reported by Sievers et al. (2015) further confirm that significant fluid-mediated metasomatism was required to produce the selvage.

Our oxygen isotope data provide us with additional leverage to estimate the amount of water that was required to produce the selvage (Fig. 6B). The selvage has the highest $\delta^{18}O$ of any lithology in the traverse (Fig. 6B). This observation is at odds with a closed system interpretation for formation of the selvage (e.g., Fig. 2A). Since all rocks have comparable concentrations of oxygen, reaction of the eclogite with the host gneiss would be expected to produce an oxygen isotope composition for the selvage that was intermediate between that of the host gneiss and eclogite. With the likely protolith for the eclogite being a basalt, it is reasonable to anticipate that its initial whole rock $\delta^{18}O$ would have been similar to the oxygen isotope composition of unaltered basalts worldwide (ca. 5–7‰; Bindeman, 2008) and ion microprobe garnet $\delta^{18}O$ values from eclogite samples from the traverse are indeed consistent with a ca. 6‰ whole rock $\delta^{18}O$ value (Menold and Grove, 2015). This mantle-like composition indicates that the eclogite's protolith could not have contributed ^{18}O-enriched fluid to form the selvage. While it is uncertain whether the gneiss's protolith was igneous, sedimentary, or of mixed origin (Gehrels et al., 2003; Zhang et al., 2013), the gneiss presently has a whole rock oxygen isotope composition of about 13‰ (Fig. 6B). Hence if the selvage was formed by closed system reaction of the eclogite and host gneiss in 1:1 proportions (Fig. 5A; see Table DR2 in the Data Repository) the resulting whole rock $\delta^{18}O$ of the selvage would be ca. 9.5‰ rather than 13–14‰ (Fig. 6B).

Below we apply Taylor's (1977, pp. 523–524) one dimensional expression for closed system fluid–rock exchange ($W/R = [\delta^{f}_{rock} - \delta^{i}_{rock}]/[\delta^{i}_{water} - (\delta^{f}_{rock} + \Delta)]$) to estimate how much external high $\delta^{18}O$ fluid would have been required to elevate the selvage whole rock $\delta^{18}O$ from 9.5‰ to its observed value of 13–14‰ (Fig. 9). These calculations assume a water/rock fractionation factor based upon plagioclase–water ($\Delta = 2.68(10^6/T^2) - 3.53$) and an equilibration temperature of 607 °C for selvage formation. Because Taylor's model assumes 100% equilibration of fluid with the rock, the calculation provides a minimum bound upon the extent of fluid–rock interaction required to produce the observed oxygen isotope composition of the selvage. The three curves shown in Fig. 9 represent solutions to Taylor's (1977) "closed beaker" model for water/rock interaction for initial $\delta^{18}O$ values of the infiltrating fluid ranging from 13 to 15‰. As indicated in Fig. 8, water/rock ratios well in excess of unity are required to match the observed whole rock $\delta^{18}O$ composition of the selvage. Moreover, less ^{18}O enriched fluid (e.g., <13‰) would be incapable of generating the $\delta^{18}O$ composition of the selvage.

Our ion probe measurements of $\delta^{18}O$ in zircon from the host gneiss provide strong evidence that it was also affected by infiltration of the heavy $\delta^{18}O$ fluid that formed the selvage. Zircon is among the phases that resist fluid-induced alteration most strongly (Bindeman, 2008). The interiors of zircon grains present within the gneiss sample furthest from the eclogite (CM 7/17/02-1) preserve $\delta^{18}O$ values between 5 and 7‰ (Fig. 7A). We interpret the significantly heavier $\delta^{18}O$(9.7‰) metamorphic rims developed on this grains to reflect interaction with a heavy $\delta^{18}O$ fluid (Fig. 7B). Our interpretation is further supported by results from selvage (CM 7/17/02-7) which primarily contains metamorphic zircon that yields $\delta^{18}O$ values between 8.5 and 11‰ (Fig. 7A).

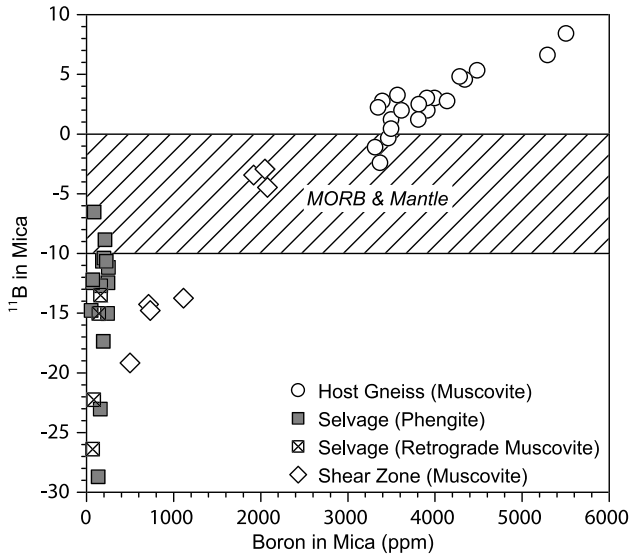

Fig. 8. Boron concentration vs. δ^{11}B isotopic values from the traverse. Selvage phengites exhibit low boron concentrations and negative δ^{11}B values with retrograde muscovite yielding the lowest values. Muscovites from the host gneiss and a shear zone cutting the selvage yield very high boron concentrations and positive δ^{11}B values.

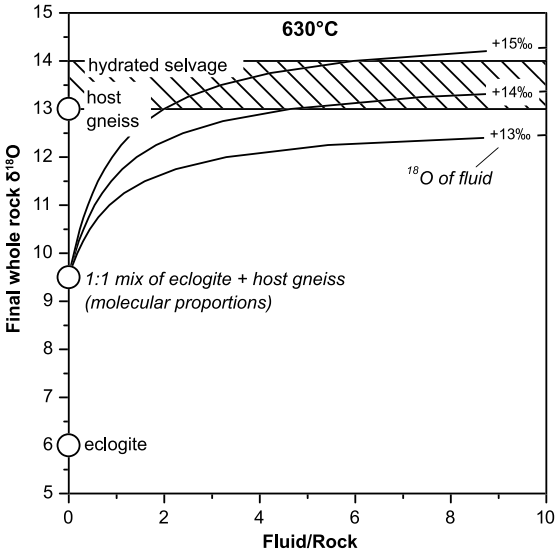

Fig. 9. Oxygen isotope modeling results. Calculations assume complete equilibration of infiltrating fluid with the selvage as described in the text. The initial starting composition of the selvage is considered to be a 1:1 mixture of host gneiss and eclogite ($\delta^{18}O = 9$; see text; Table 1). Solutions provided for fluids with initial $\delta^{18}O = 13‰$, 14‰, and 15‰. Water/rock values indicate the minimum amount of fluid required to increase the selvage δ^{18}O from 9‰ to final composition (13‰ to 14‰).

Our results do not uniquely constrain the origin of the high δ^{18}O fluids. The Luliang Shan gneiss could well have acquired its high δ^{18}O composition from a sedimentary protolith. In this case, heavy δ^{18}O fluids devolatilized from gneiss can account for the development of heavy δ^{18}O rims upon lower δ^{18}O detrital zircons. However, analysis of the devolatilization history of bulk compositions similar to the gneiss indicate that metagranite bulk compositions do not easily recrystallize under HP to UHP conditions and ca. 600 °C temperatures without the influx of external fluids (e.g., Proyer, 2003; Massonne, 2009). In sediment-rich subduction settings, fluids with δ^{18}O values as high as ca. 14‰ are characteristically devolatilized from lower temperature metasediments (Margaritz and Taylor, 1976). These high δ^{18}O fluids are available to infiltrate higher temperature rocks accreted to the base of the mantle lithosphere (Bebout and Barton, 2002). While most metasedimentary rocks are devolatilized at shallower depths than the 80 km depths represented by the Luliang Shan (e.g., Schmidt and Poli, 1998), secondary processes advect the high δ^{18}O signature imparted by low-grade sediment devolatilization to greater depths within the subduction zone. For example, mantle lithosphere hydrated at shallower depths to produce high δ^{18}O chlorite–amphibole–serpentine-bearing assemblages (e.g., Bebout and Barton, 2002) may be sheared downward by subducting oceanic crust to 80 km depths where devolatilization takes place (Schmidt and Poli, 1998; Pawley, 2003; Till et al., 2012).

Boron is expected to be enriched in devolatilized fluids and depleted in the corresponding host rocks with boron isotopic values providing a sensitive indication of the extent of devolatilization (Bebout, 2007; Marschall et al., 2007). Our boron isotope measurements thus bear directly upon the issue of whether the selvage could have been formed from fluids devolatilized directly from adjacent host gneiss (Fig. 1B). For example, if the source of selvage-forming fluid was derived from immediately adjacent host gneiss and all of the transferred fluid was consumed during selvage formation, then boron concentrations and δ^{11}B values should be comparable in both the selvage and the host gneiss. In fact, the boron concentrations and δ^{11}B values of the selvage phengites and the host gneiss muscovites could not be more different (Fig. 8). The selvage phengites exhibit boron concentrations up to 250 ppm and negative δ^{11}B values that are generally below the range of δ^{11}B values exhibited by MORB basalts and the mantle (Fig. 8). Such values are characteristic of fluid sourced from highly devolatilized source rocks (Marschall et al., 2007). In contrast, the host gneiss muscovites had extremely high boron concentrations (up to 5500 ppm) and δ^{11}B values that are generally more positive than MORB and mantle values (Fig. 8). These observations coupled with the existence of tourmaline in CM 7/17/02-1 are much more evocative of "blackwall-style" metasomatism produced by lower temperature and lower pressure subduction-related fluids (e.g., Marschall et al., 2007) compared to the source region that produced boron poor, and much more negative δ^{11}B fluids in the selvage. Given likely phengite/fluid partition coefficients for boron and the fractionation effects upon boron isotopes (Marschall et al., 2007), the only way to reconcile the contrast in boron concentrations and δ^{11}B values exhibited by the host gneiss and the selvage would be for the majority of the fluid devolatilized from the gneiss to have migrated away from the selvage. In fact there is no evidence that fluids in equilibrium with host gneiss muscovites ever equilibrated with the selvage phengites. For example, while the host gneiss muscovites are highly enriched in B relative to the selvage phengites, they are depleted in other incompatible trace elements relative to the selvage phengites. Sievers et al. (2015) report that the selvage phengites contain appreciable Li (to 700 ppm), Cs (to 80 ppm), and Ba (to 2000 ppm) while the host gneiss muscovites have much lower concentrations of these elements (up to 130 ppm, 40 ppm, and 100 ppm respectively).

Given these significant discrepancies in incompatible trace element composition, it is simplest to conclude that the histories of fluid interaction recorded by the selvage phengites and host gneiss muscovites were fundamentally decoupled. We consider it most likely that the host gneiss was essentially anhydrous at the time of selvage formation and that the muscovite and tourmaline presently observed in the gneiss are retrograde phases formed during the 0.8–0.9 GPa and 415–510 °C epidote amphibolite conditions that were encountered by the gneiss along its exhumation path (Menold et al., 2009). Sievers et al. (2015) attributed the source of the late-stage high boron and positive δ^{11}B fluids to devolatilization of the shallower region of a subduction channel that

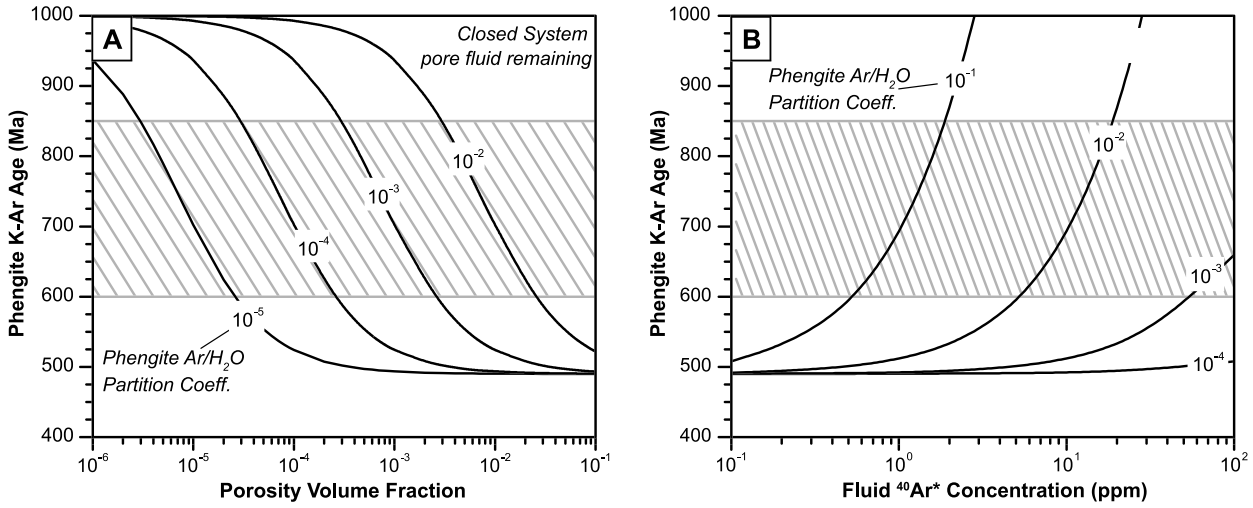

Fig. 10. Excess ^{40}Ar ($^{40}Ar_E$) model results. A. Phengite K–Ar ages calculated assuming a closed system and that residual water remains in the intergranular region after selvage formation. Solutions calculated as a function of porosity volume fraction. Labeled curves represent solutions for different phengite Ar/fluid partition coefficients. B. Phengite K–Ar ages calculated an open system in which the argon concentration of the fluid remains constant. Solutions are shown for different Phengite Ar/fluid partition coefficients.

the Luliang Shan gneiss terrane moved past as it was exhumed towards the surface (e.g., Marshall et al., 2007).

In summary, our whole rock geochemistry, $\delta^{18}O$, and $\delta^{11}B$ data provide strong and self-consistent evidence that selvage formation within the Luliang Shan occurred at reactive eclogite–gneiss contacts in response to regional-scale infiltration of (possibly subduction-derived) high $\delta^{18}O$ fluids at pressures near the coesite stability field (605 °C at 25 kbar; Menold et al., 2009). Our conclusion that selvages formed around eclogite in response to regional fluid flow rather than local exchange between adjacent lithologies (Fig. 2) is consistent with the results of studies such as Proyer (2003) and Massonne (2009) that have shown that metagranite bulk compositions are not prone to recrystallize at ca. 600 °C temperatures and HP to UHP depths unless infiltrated by fluid.

5.2. Controls on $^{40}Ar_E$ accumulation in phengite during high-pressure metamorphism

The expectation of low phengite/fluid partition coefficients for argon (10^{-3} to 10^{-6}; e.g., Kelley, 2002) coupled with petrographic and isotopic evidence for low a_{H2O} and limited fluid flow during HP to UHP metamorphism of continental crust (Philippot, 1993; Rumble and Yui, 1998) have formed the basis for the interpretation that dry conditions during HP to UHP metamorphism cause high concentrations of $^{40}Ar_E$ to build up in undeformed, phengite (e.g., Scaillet, 1998; Kelley, 2002; Cosca et al., 2005, 2011; Warren et al., 2012; Smye et al., 2013). The inability of argon to diffuse out of phengite and/or the ability for phengite to incorporate $^{40}Ar_E$ from surrounding phases at high pressures has been attributed to the greatly diminished capacity of the intergranular region to sequester argon from minerals in low porosity and permeability rocks such as eclogite (e.g., Smye et al., 2013).

Fig. 10A is based upon a conceptual approach developed by Smye et al. (2013) to predict the relationship between porosity and $^{40}Ar_E$ accumulation in phengite under closed system conditions with pore fluid present in the intergranular region. The model is valid for conditions where temperature is high enough to permit argon to freely diffuse from phengite into the fluid phases and vice versa. The magnitude of the phengite–fluid partition coefficient ($D^{Ar}_{phg/fl}$) determines the relative proportions of argon in phengite and fluid. As indicated in Fig. 10A, the amount of $^{40}Ar_E$ that accumulated in phengite should be higher in low porosity lithologies like eclogite since less pore fluid is available. Conversely, selvage phengites are expected to have lower $^{40}Ar_E$, and thus yield younger total gas $^{40}Ar/^{39}Ar$ ages because more pore fluid is available and low values of $D^{Ar}_{phg/fl}$ cause argon to strongly prefer the fluid phase.

Closed system partitioning of $^{40}Ar_E$ between phengite and pore fluid within the intergranular region depicted in Fig. 10A cannot explain the distribution of $^{40}Ar/^{39}Ar$ total gas ages along the traverse. Specifically, while the phengite total gas $^{40}Ar/^{39}Ar$ ages measured from the massive eclogites were up to 150% higher than the 488 Ma zircon U–Pb ages for the timing of eclogite metamorphism (Zhang et al., 2005), our study documented concentrations of $^{40}Ar_E$ that produced ages up to 170% higher than the age of eclogite metamorphism in the selvage phengites (Fig. 6A). Combined with the oxygen and boron isotope data discussed above, the fact that more $^{40}Ar_E$ accumulated in phengite under the more fluid-rich conditions within the selvage than the more fluid-poor conditions of the eclogite clearly indicates open system behavior during selvage formation.

In an open system, the magnitude of the Ar/fluid partition coefficient and the concentration of $^{40}Ar_E$ in the fluid determine how much $^{40}Ar_E$ can be incorporated within phengite (Fig. 10B). As indicated in Fig. 10B, values for $D^{Ar}_{phg/fl}$ between 10^{-2} and 10^{-3} coupled with argon concentrations (C^{Ar}_{fl}) of 10–100 ppm are required to account for phengite K–Ar ages from the selvage. The magnitudes of both the concentration of argon in the fluid and the partition coefficient required to explain our results in an open system could be considered problematic because they exceed existing estimates. For example, fluid inclusion studies of crustal rocks (e.g., Harrison et al., 1994) have suggested an upper limit of 50 ppm for Ar in fluid. More significantly, many authors have concluded that phengite/fluid partition coefficients for argon must be low (e.g., 10^{-3} to 10^{-5}; Kelley, 2002) to force appreciable $^{40}Ar_E$ from the fluid phase into phengite under perceived dry conditions (e.g., Warren et al., 2012). We propose that higher $^{40}Ar_E$ content in phengites that have experienced greater fluid–rock interaction makes sense if partition coefficients increase with pressure in the same manner as argon solubilities do (i.e., Henry's Law behavior). For example, a linear pressure dependence of the form $D^{Ar}_{phg/fl} = 1 \times 10^{-5} + 0.06P$ (GPa) could produce $D^{Ar}_{phg/fl}$ values as high as 10^{-2} at 7.5 GPa pressures.

Pressure-dependent increase in $D^{Ar}_{phg/fl}$ is consistent with experimental evidence that the solubility of argon in melts of various compositions increases systematically as a function of pressure

(Carroll and Stolper, 1993). More significantly, while argon and other noble gases are consider highly incompatible elements at low-pressure crustal conditions, high-pressure experiments simulating mantle melting have revealed that argon behaves as a more "compatible" element at high-pressures that remains in mantle phases rather than being overwhelmingly "flushed" into melts, although conflicting results have been obtained (Hiyagon and Ozima, 1986; Broadhurst et al., 1990; cf. Chamorro et al., 2002; Brooker et al., 2003). Regardless, lower temperature and pressure experiments are required to more confidently constrain the phengite–fluid partitioning behavior under HP to UHP conditions.

5.3. Conclusions

Our field, petrographic, compositional and isotopic evidence from the Luliang Shan locality of the North Qaidam UHP terrane yield the following conclusions. (1) Our whole rock geochemistry, $\delta^{18}O$, and $\delta^{11}B$ data provide strong and self-consistent evidence that selvage formation within the Luliang Shan occurred at reactive eclogite–gneiss contacts in response to regional-scale infiltration of (possibly subduction-derived) high $\delta^{18}O$, low $\delta^{11}B$ fluids at pressures near the coesite stability field (605 °C at 25 kbar; Menold et al., 2009). (2) The source of the late-stage high boron and positive $\delta^{11}B$ fluids was of the shallower region of a subduction channel that the Luliang Shan gneiss terrane moved past as it was exhumed towards the surface. (3) The presence of large quantities of $^{40}Ar_E$ in phengite in the HP metasomatic selvage suggest that phengite/fluid partition coefficients for argon increase linearly with pressure to values as high as 10^{-2}.

Acknowledgements

The work was supported by National Science Foundation Grant EAR-03-37191 and Albion College Faculty Development Funds. The ion microprobe facility at UCLA is partly supported by a grant from the Instrumentation and Facilities Program, Division of Earth Sciences, National Science Foundation. We would like to thank Rita Economos and Axel Schmidt for their assistance on the SIMS at UCLA. We would also like to thank Matt Coble for his assistance on the SHRIMP-RG at the USGS/Stanford University facility. We thank Zeb Page for comments on an earlier version of this manuscript.

Appendix A. Supplementary material

Supplementary material related to this article can be found online at http://dx.doi.org/10.1016/j.epsl.2016.04.010.

References

Baxter, E.F., DePaolo, D.J., Renne, P.R., 2002. Spatially correlated anomalous $^{40}Ar/^{39}Ar$ "age" variations in biotites about a lithologic contact near Simplon Pass, Switzerland: a mechanistic explanation for excess Ar. Geochim. Cosmochim. Acta 66, 1067–1083. http://dx.doi.org/10.1016/S0016-7037(01)00828-6.

Bebout, G.E., Barton, M.D., 2002. Tectonic and metasomatic mixing in a high-T, subduction-zone mélange—insights into the geochemical evolution of the slab-mantle interface. Chem. Geol. 187, 79–106. http://dx.doi.org/10.1016/S0009-2541(02)00019-0.

Bebout, G.E., 2007. Metamorphic chemical geodynamics of subduction zones. Earth Planet. Sci. Lett. 260, 373–393. http://dx.doi.org/10.1016/j.epsl.2007.05.050.

Bindeman, I., 2008. Oxygen isotopes in mantle and crustal magmas as revealed by single crystal analysis. Rev. Mineral. Geochem. 69, 445–478. http://dx.doi.org/10.2138/rmg.2008.69.12.

Brand, W.A., Coplen, T.B., Vogl, J., Rosner, M., Prohaska, T., 2014. Assessment of international reference materials for isotope-ratio analysis (IUPAC Technical Report). Pure Appl. Chem. 86 (3), 425–467. http://dx.doi.org/10.1515/pac-2013-1023.

Broadhurst, C.L., Drake, M.J., Hagee, B.E., Bernatowicz, T.J., 1990. Solubility and partitioning of Ar in anorthite, diopside, forsterite, spinel, and synthetic basaltic liquids. Geochim. Cosmochim. Acta 54, 299–309. http://dx.doi.org/10.1016/0016-7037(90)90319-G.

Brooker, R.A., Du, Z., Blundy, J.D., Kelley, S.P., Allan, N.L., Wood, B.J., Chamarro, E.M., Wartho, J.-A., Purton, J.A., 2003. The 'zero charge' partitioning behavior of noble gases during mantle melting. Nature 423, 738–741. http://dx.doi.org/10.1038/nature01708.

Cagnioncle, A.M., Parmentier, E.M., Elkins-Tanton, L.T., 2007. Effect of solid flow above a subducting slab on water distribution and melting at convergent plate boundaries. J. Geophys. Res. 112, B09402. http://dx.doi.org/10.1029/2007JB004934.

Carroll, M.R., Stolper, E.M., 1993. Noble gas solubilities in silicate melts and glasses: new experimental results for argon and the relationship between solubility and ionic porosity. Geochim. Cosmochim. Acta 57, 5039–5051. http://dx.doi.org/10.1016/0016-7037(93)90606-W.

Chamorro, E.M., Brooker, R.A., Wartho, J.-A., Wood, B.J., Kelley, S.P., Blundy, J.D., 2002. Ar and K partitioning between clinopyroxene and silicate melt to 8 GPa. Geochim. Cosmochim. Acta 66, 507–519. http://dx.doi.org/10.1016/S0016-7037(01)00784-0.

Cosca, M.A., Giorgis, D., Rumble, D., Liou, J.G., 2005. Limiting effects of UHP metamorphism on length scales of oxygen, hydrogen, and argon isotope exchange: an example from the Qinglongshan UHP eclogites, Sulu terrane, China. Int. Geol. Rev. 47, 716–749. http://dx.doi.org/10.2747/0020-6814.47.7.716.

Cosca, M., Stunitz, H., Bourgeix, A.-L., Lee, J.P., 2011. $^{40}Ar^*$ loss in experimentally deformed muscovite and biotite with implications for $^{40}Ar/^{39}Ar$ geochronology of naturally deformed rocks. Geochim. Cosmochim. Acta 75, 7759–7778. http://dx.doi.org/10.1016/j.gca.2011.10.012.

Gehrels, G.E., Yin, A., Wang, X.-F., 2003. Magmatic history of the northeastern Tibetan Plateau. J. Geophys. Res. 108 (B9), 2423. http://dx.doi.org/10.1029/202JB001876.

Halama, R., Konrad-Schmolke, M., Sudo, M., Marschall, H.R., Wiedenbeck, M., 2014. Effects of fluid–rock interaction on $^{40}Ar/^{39}Ar$ geochronology in high-pressure rocks (Sesia-Lanzo Zone, Western Alps). Geochim. Cosmochim. Acta 126, 475–494. http://dx.doi.org/10.1016/j.gca.2013.10.023.

Harrison, T.M., Heizler, M.T., Lovera, O.M., Chen, W.J., Grove, M., 1994. A chlorine disinfectant for excess argon released from K-feldspar during step-heating. Earth Planet. Sci. Lett. 123, 95–104. http://dx.doi.org/10.1016/0012-821X(94)90260-7.

Hiyagon, H., Ozima, M., 1986. Partition of noble gases between olivine and basalt. Geochim. Cosmochim. Acta 50, 2045–2057. http://dx.doi.org/10.1016/0016-7037(86)90258-9.

Ishikawa, T., Nakamura, E., 1994. Origin of the slab component in arc lavas from across-arc variation of B and Pb isotopes. Nature 370, 205–208. http://dx.doi.org/10.1038/370205a0.

Iwamori, H., 1998. Transportation of H_2O and melting in subduction zones. Earth Planet. Sci. Lett. 160, 65–80. http://dx.doi.org/10.1016/S0012-821X(98)00080-6.

Jourdan, F., Renne, P.R., 2007. Age calibration of the Fish Canyon sanidine $^{40}Ar/^{39}Ar$ dating standard using primary K–Ar standards. Geochim. Cosmochim. Acta 71, 387–402. http://dx.doi.org/10.1016/j.gca.2006.09.002.

Kelley, S., 2002. Excess argon in K–Ar and Ar–Ar geochronology. Chem. Geol. 188, 1–22. http://dx.doi.org/10.1016/S0009-2541(02)00064-5.

Kylander-Clark, A.R.C., Hacker, B.R., Mattinson, C.G., 2012. Size and exhumation rate of ultrahigh-pressure terranes linked to orogenic stage. Earth Planet. Sci. Lett. 321–322, 115–120.

Lovera, O.M., Grove, M., Harrison, T.M., Mahon, K.I., 1997. Systematic analysis of K-feldspar $^{40}Ar/^{39}Ar$ step heating results: I. Significance of activation energy determinations. Geochim. Cosmochim. Acta 61, 3171–3192. http://dx.doi.org/10.1016/S0016-7037(97)00147-6.

Manning, C.E., 2004. The chemistry of subduction-zone fluids. Earth Planet. Sci. Lett. 223, 1–16. http://dx.doi.org/10.1016/j.epsl.2004.04.030.

Margaritz, M., Taylor, H.P., 1976. Oxygen, hydrogen and carbon isotope studies of the franciscan formation, Coast Ranges California. Geochim. Cosmochim. Acta 40, 215–234. http://dx.doi.org/10.1016/0016-7037(76)90179-4.

Marschall, H.R., Altherr, R., Rüpke, L., 2007. Squeezing out the slab — modelling the release of Li, Be and B during progressive high-pressure metamorphism. Chem. Geol. 239, 223–235. http://dx.doi.org/10.1016/j.chemgeo.2006.08.008.

Massonne, H.-J., 2009. Hydration, dehydration, and melting of metamorphosed granitic and dioritic rocks at high- and ultrahigh-pressure conditions. Earth Planet. Sci. Lett. 288, 244–254. http://dx.doi.org/10.1016/j.epsl.2009.09.028.

Mattinson, C.G., Menold, C.A., Zhang, J.X., Bird, D.K., 2007. High- and ultrahigh-pressure metamorphism in the North Qaidam and South Altyn Terranes, Western China. Int. Geol. Rev. 49, 969–995. http://dx.doi.org/10.2747/0020-6814.49.11.969.

Menold, C.A., Manning, C.E., Yin, A., Tropper, P., Chen, X.-H., Wang, X.-F., 2009. Metamorphic evolution, mineral chemistry and thermobarometry of gneiss hosting ultrahigh-pressure eclogites in the North Qaidam metamorphic belt, Western China. J. Asian Earth Sci. 35, 273–284. http://dx.doi.org/10.1016/j.jseaes.2008.12.008.

Menold, C.A., Grove, M., 2015. Oxygen isotope evidence of subduction zone fluid metasomatism during UHP metamorphism. In: GSA Fall Meeting. Baltimore, MD.

Pawley, A., 2003. Chlorite stability in mantle peridotite: the reaction clinochlore + enstatite = forsterite + pyrope + H_2O. Contrib. Mineral. Petrol. 144, 449–456. http://dx.doi.org/10.1007/s00410-002-0409-y.

Philippot, P., 1993. Fluid–melt–rock interaction in mafic eclogites and coesite-bearing metasediments: constraints on volatile recycling during subduction. Chem. Geol. 108, 93–112. http://dx.doi.org/10.1016/0009-2541(93)90319-E.

Proyer, A., 2003. The preservation of high-pressure rocks during exhumation: metagranites and metapelites. Lithos 70, 183–194. http://dx.doi.org/10.1016/S0024-4937(03)00098-7.

Richter, R., Hoernes, S., 1988. The application of the increment method in comparison with experimentally derived and calculated O-isotope fractionations. Chem. Erde 48, 1–18.

Rumble, D., Yui, T.-F., 1998. The Qinglongshan oxygen and hydrogen isotope anomaly near Donghai in Jiangsu Province, China. Geochim. Cosmochim. Acta 62, 3307–3321. http://dx.doi.org/10.1016/S0016-7037(98)00239-7.

Scaillet, S., 1998. K–Ar ($^{40}Ar/^{39}Ar$) geochronology of ultrahigh-pressure rocks. In: Hacker, B.R., Liou, J.G. (Eds.), When Continents Collide: Geodymanics and Geochemistry of Ultrahigh-Pressure Rocks. Kluwer Acad. Publ., pp. 161–201.

Schmidt, M.W., Poli, S., 1998. Experimentally based water budgets for dehydrating slabs and consequences for arc magma generation. Earth Planet. Sci. Lett. 163, 361–379. http://dx.doi.org/10.1016/S0012-821X(98)00142-3.

Sievers, N.E., Menold, C., Grove, M., 2015. Trace element variations as indicators of fluid sources and infiltration history during UHP metamorphism of continental crust. In: Presented at the 48th Annual Meeting of the American Geophysical Union. San Francisco, CA.

Smye, A.J., Warren, C.J., Bickle, M.J., 2013. The signature of devolatisation: extraneous ^{40}Ar systematics in high-pressure metamorphic rocks. Geochim. Cosmochim. Acta 113, 94–112. http://dx.doi.org/10.1016/j.gca.2013.03.018.

Taylor, H.P., 1977. Water/rock interactions and the origin of H_2O in granitic batholiths. J. Geol. Soc. (Lond.) 133, 509–558. http://dx.doi.org/10.1144/gsjgs.133.6.0509.

Till, C.B., Grove, T.L., Withers, A.C., 2012. The beginnings of hydrous mantle wedge melting. Contrib. Mineral. Petrol. 163 (4), 669–688.

Trail, D., Mojzsis, S.J., Harrison, T.M., Schmitt, A.K., Watson, E.B., Young, E.D., 2007. Constraints on Hadean zircon protoliths from oxygen isotopes, Ti-thermometry, and rare earth elements. Geochem. Geophys. Geosyst. 8. http://dx.doi.org/10.1029/2006GC001449.

Warren, C.J., Smye, A.J., Kelley, S.P., Sherlock, S.C., 2012. Using white mica $^{40}Ar/^{39}Ar$ data as a tracer for fluid flow and permeability under high-P conditions: Tauern Window, Eastern Alps. J. Metamorph. Geol. 30, 63–80. http://dx.doi.org/10.1111/j.1525-1314.2011.00956.x.

Yang, J.S., Xu, Z.Q., Zhang, J.X., Song, S.G., Wu, C.L., Shi, R.D., Li, H.B., Brunel, M., 2002. Early Paleozoic North Qaidam UHP metamorphic belt on the northeastern Tibetan plateau and a pair subduction model. Terra Nova 14, 397–404. http://dx.doi.org/10.1046/j.1365-3121.2002.00438.x.

Yin, A., Manning, C.E., Lovera, O., Menold, C.A., Chen, X.-H., Gehrels, G.E., 2007. Early Paleozoic tectonic and thermomechanical evolution of ultrahigh-pressure (UHP) metamorphic rocks in the Northern Tibetan plateau, northwest China. Int. Geol. Rev. 49, 681–716. http://dx.doi.org/10.2747/0020-6814.49.8.681.

Yin, A., Dang, Y.-Q., Wang, L.-C., Jiang, W.-M., Zhou, S.-P., Chen, X.-H., Gehrels, G.E., McRivette, M.W., 2008. Cenozoic tectonic evolution of Qaidam basin and its surrounding regions (Part 1): the southern Qilian Shan-Nan Shan thrust belt and northern Qaidam basin. Geol. Soc. Am. Bull. 120, 813–846. http://dx.doi.org/10.1130/B26180.1.

Young, E.D., Nagahara, H., Mysen, B.O., Audet, D.M., 1998. Non-Rayleigh oxygen isotope fractionation by mineral evaporation: theory and experiments in the system SiO_2. Geochim. Cosmochim. Acta 62, 3109–3116. http://dx.doi.org/10.1016/S0016-7037(98)00213-0.

Zhang, G., Zhang, L., Song, S., Niu, Y., 2009. UHP metamorphic evolution and SHRIMP geochronology of a coesite-bearing meta-ophiolitic gabbro in the North Qaidam, NW China. J. Asian Earth Sci. 35, 310–322. http://dx.doi.org/10.1016/j.jseaes.2008.11.013.

Zhang, G., Zhang, L., Christy, A.G., 2013. From oceanic subduction to continental collision: an overview of HP-UHP metamorphic rocks in the North Qaidam UHP belt, NW China. J. Asian Earth Sci. 63, 98–111. http://dx.doi.org/10.1016/j.jseaes.2012.07.014.

Zhang, J.X., Yang, J.S., Mattinson, C.G., Xu, Z.Q., Meng, F.C., Shi, R.D., 2005. Two contrasting eclogite cooling histories, North Qaidam HP/UHP terrane, western China: petrological and isotopic constraints. Lithos 84, 51–76. http://dx.doi.org/10.1016/j.lithos.2005.02.002.

Zheng, X.-F., 1993. Calculation of oxygen isotope fractionation in hydroxyl-bearing silicates. Earth Planet. Sci. Lett. 120, 247–263. http://dx.doi.org/10.1016/0012-821X(93)90243-3.